Received: 24 May 2021 | Revised: 2 September 2021 | Accepted: 21 September 2021

DOI: 10.1002/aic.17454

FUTURES ISSUE: REACTION ENGINEERING, KINETICS AND CATALYSIS

AIChE JOURNAL

Modeling phase formation on catalyst surfaces: Coke formation and suppression in hydrocarbon environments

Peng Wang | **Thomas P. Senftle**

Department of Chemical and Biomolecular Engineering, Rice University, Houston, Texas, USA

Correspondence
Thomas P. Senftle, Department of Chemical and Biomolecular Engineering, Rice University, Houston, TX 77005, USA.
Email: tsenftle@rice.edu

Funding information
American Chemical Society Petroleum Research Fund, Grant/Award Number: PRF #59759-DNI6

Abstract

We develop a simulation toolset employing density functional theory in conjunction with grand canonical Monte Carlo (GCMC) to study coke formation on Fe-based catalysts during propane dehydrogenation (PDH). As expected, pure Fe surfaces develop stable graphitic coke structures and rapidly deactivate. We find that coke formation is markedly less favorable on Fe_3C and FeS surfaces. Fe-Al alloys display varying degrees of coke resistance, depending on their composition, suggesting that they can be optimized for coke resistance under PDH conditions. Electronic structure analyses show that both electron-withdrawing effects (on Fe_3C and FeS) and electron-donating effects (on Fe-Al alloys) destabilize adsorbed carbon. On the alloy surfaces, a geometric effect also isolates Fe sites and disrupts the formation of graphitic carbon networks. This work demonstrates the utility of GCMC for studying the formation of disordered phases on catalyst surfaces and provides insights for improving the coke resistance of Fe-based PDH catalysts.

KEYWORDS
catalysis, computational chemistry (at solid surfaces), computer simulations (MC and MD), hydrocarbon processing, molecular, simulation

1 | INTRODUCTION

Catalyst behavior and performance often is impacted by the in situ formation of secondary phases on catalyst surfaces under reaction conditions. The effect of such phase formation is observed clearly when a catalyst displays a so-called *induction period* in which reaction activity or selectivity rapidly evolves over the initial moments after exposure to the reaction environment.[1–4] There are numerous examples in the literature demonstrating how catalysis is affected by the formation of bulk oxides,[5] carbides,[6] hydrides,[7] or sulfides,[8] which are fairly easy to identify through in situ characterization. A more challenging problem is the identification of surface phase transitions that, compared to bulk phase transitions, only involve the rearrangement of the first few atomic layers of the catalyst surface. Ex situ characterization of the catalyst postreaction is less reliable for determining the surface state of the catalyst under reaction conditions, as surface structures are altered more readily than bulk structures when taken out of the reaction environment. As a result, in situ characterization has become a popular topic for capturing the interplay between catalysts and reactants, yet there are still practical limitations inherent to these methods.[9,10] Atomistic modeling and simulation can offer complementary insight into the formation of surface phases under reactions conditions.

One of the most common approaches for deriving theoretical phase diagrams is the formalism of ab initio thermodynamics. An early application of this method in catalysis was developed by Reuter and Scheffler,[11] who used ab initio thermodynamics to investigate the relative stability of different surface structures of RuO_2(110). They derived the free energy of surfaces with varying amounts of adsorbed oxygen as a function of the oxygen chemical potential, which in turn was used to predict the state of the surface as a function of temperature and oxygen pressure. Having established the state of the surface under reaction conditions, they then could explore its catalytic behavior during CO oxidation.[12,13] These methods have been implemented

widely in the literature on many different systems,[14] such as carbides[15] and semiconductors.[16–18] While powerful, this formalism is limited by the fact that the surface structures considered in the analysis must be populated a priori from physical intuition. Simply cleaving different facet terminations from the bulk structure will neglect reconstructions of the surface that are often quite stable. Therefore, reconstructions must be anticipated from intuition (i.e., experience) or from experimental evidence (if it is available). Identifying relevant reconstructions becomes increasingly difficult when studying the formation of disordered structures, such as the formation of coke on a catalyst surface, and automated procedures for effectively sampling the configurational phase space are required.

Grand canonical Monte Carlo (GCMC) is a method that can be utilized to explore the formation of surface structures without a priori knowledge of the system's behavior. In a GCMC simulation, the system is permitted to exchange atoms with a theoretical reservoir at a reference chemical potential. Monte Carlo (MC) moves feature the insertion, removal, and displacement of atoms in the system, which allows the simulation to effectively explore the phase diagram.[19] The probability of move acceptance, which is derived from rigorous statistical thermodynamics, ensures that the simulation samples the stable region of the phase diagram under a given set of conditions. Thus, the simulation is populated by an ensemble of structures with high relevance to the reaction conditions (i.e., temperature and gas phase composition). GCMC has been utilized successfully to study phase formation in hydrogen storage materials[20–22] and surface adsorption on zeolites.[23] We have previously developed an implementation of a hybrid GCMC-MD algorithm with the ReaxFF force field[24] to study the oxidation of metallic Pd surfaces and clusters,[25,26] and the formation of Pd hydrides[27] and carbides.[28] This code was also used to predict the oxidation phase diagrams of Pt(111) surfaces and clusters, which were corroborated by experimental observations.[29,30] Similarly, Gai et al.[31] applied the GCMC/ReaxFF method to investigate the adsorption of O and H on Pt surfaces and particles. Wexler et al.[32] developed a similar strategy, where they combined GCMC with density functional theory (DFT) (instead of ReaxFF) to simulate oxide formation on the Ag(111) surface. They used this approach not only to explore the phase diagram, but also to better understand the oxide formation process by identifying the intermediate stages of surface oxide formation, which featured Ag_3O_4 pyramids and an $Ag_{10}O_7$ overlayer, in agreement with experiment.

In this work, we develop and extend tool sets for applying GCMC in tandem with DFT for studying surface phase formation. This tool set is applied to better understand coke formation and suppression on Fe-based catalysts. Coke formation on catalyst surfaces is a major cause of catalyst deactivation in several industrial reactions involving hydrocarbon-rich environments, such as Fischer–Tropsch synthesis,[33–36] methane reforming,[37–40] CO_2 reduction,[41] fluid catalytic cracking,[42,43] and hydrocarbon dehydrogenation.[44,45] Various strategies have been developed to suppress coke formation, typically by adding promoters and dopants,[46–48] forming metal phosphides or sulfides,[49–52] forming nitrides or carbides,[44,53] or alloying with less carbophilic metals.[54–56] The particular interest in this work is the suppression of coke formation during nonoxidative propane dehydrogenation (PDH). PDH has become attractive for filling the growing gap between propene demand and production.[57–59] As an alternative for commercialized PDH catalysts based on expensive Pt or toxic Cr, Fe-based materials have drawn great attention because they are abundant and benign. Yet, Fe is highly carbophilic and suffers from rapid deactivation through coke formation under carbon-rich environments.[44,60] Various strategies have been applied to reduce coking on Fe-based catalysts. Sun et al.[46,47,61] found that coke formation can be suppressed during PDH by either adding sulfate during the catalyst preparation stage or by cofeeding SO_2 with the hydrocarbon reactants. Watanabe et al.[50,51] found that the iron sulfide formed in situ by cofeeding H_2S can suppress coke build-up. Similarly, Tan et al.[44] showed that adding phosphate during the catalyst preparation stage greatly increased the coking resistance of Fe-based PDH catalysts. In their work, they showed that an iron carbide phase forms in situ during an induction period, which coincides with increased PDH selectivity. In other examples, isolated Fe single-atom sites on silica, observed to be active by Hu et al.,[60] and dispersed Fe atoms in zeolites, reported by Sarazen and Jones,[62] showed high coke resistance during PDH. In our previous work, we found that iron carbide promotes selective PDH because it does not facilitate the cracking side reactions that lead to rapid coke formation.[63] Thus, active and selective PDH on Fe catalysts is possible if the in situ formation of coke on Fe surfaces can be suppressed.

In this work, we employ GCMC-DFT to determine the thermodynamic stability of coke formations on various Fe-based surfaces. We first perform GCMC-DFT simulations on the stable surfaces of pure iron,[44,60] iron carbide,[44] and iron sulfide,[50,51] as they all have shown different levels of coke resistance in experimental PDH studies. An alloy of iron and aluminum, $Al_{13}Fe_4$, that showed high stability during the semihydrogenation of acetylene and hydrogenation of butadiene, also is tested as a candidate PDH catalyst.[64,65] We additionally consider a 1:1 stoichiometric FeAl alloy[66] as a comparison to $Al_{13}Fe_4$ with varying composition. For each material, we chose one surface termination with high reported stability to perform the GCMC simulations. Details regarding the selected surfaces are included in the Supporting Information (Table S3). Only the chemical potentials of C and H are considered in the GCMC simulations, and therefore it is assumed that catalysts containing additives (e.g., sulfur) were preformed before being exposed to the PDH environment, which neglects possible deactivation of the catalyst through the loss of the additive (e.g., sulfur loss in the form of H_2S). Surface phase diagrams based on ab initio thermodynamics then are generated using the structures identified with GCMC. We find that several coke structures are highly stable on the pristine Fe(110) surface, which agrees with the fact that pure iron exhibits run-away coking under PDH conditions.[44] Fe_3C (010) and FeS(001) surfaces exhibit high coking resistance, where electronic structure analyses show that carbon binding on these surface is weakened because electron density on Fe is withdrawn by both C and S, which shifts the Fe d-band to a lower energy position and depopulates Fe/C bonding states. Conversely, Al was found to donate electrons to Fe on alloy surfaces, which populates

anti-bonding states and destabilizes carbon adsorption. A geometric effect also is found to be important on the Fe/Al alloys. The FeAl(110) surface exhibits greater coke resistance than Fe(110), but still can support the formation of 1D carbon chains and 2D carbon networks because rows of surface Fe atoms exposed on this facet strongly adsorb carbon and are not sufficiently isolated. The $Al_{13}Fe_4$(010) surface shows high coke resistance because all surface Fe atoms are isolated, which disrupts the formation of 2D carbon networks.

This work demonstrates how GCMC-DFT can efficiently sample the ensemble of structures that form on a catalyst surface under reaction conditions. However, the method is still limited by the computational cost of the underlying DFT calculations. For example, the size of the periodic cell is small, which yields high stress if attempting to insert subsurface carbon and also creates inherent lattice match or mismatch as the 2D carbon structures grow. The computational cost also limits the exploration of 3D carbon structures. We envision that the GCMC-DFT method also can be used to form an extensive dataset for training cheaper interatomic force-fields (Figure 1). The geometry and energy of each calculated structure (from both accepted MC moves and rejected MC moves) can serve as the input for the training of either empirical potentials (e.g., ReaxFF[24,67]) or statistical potentials (e.g., machine-learned potentials[68]). Simulations with these potentials can identify coke formation mechanisms on larger spatiotemporal scales through MC with larger system models and molecular dynamics over larger timescales, which will be the topic of our future studies.

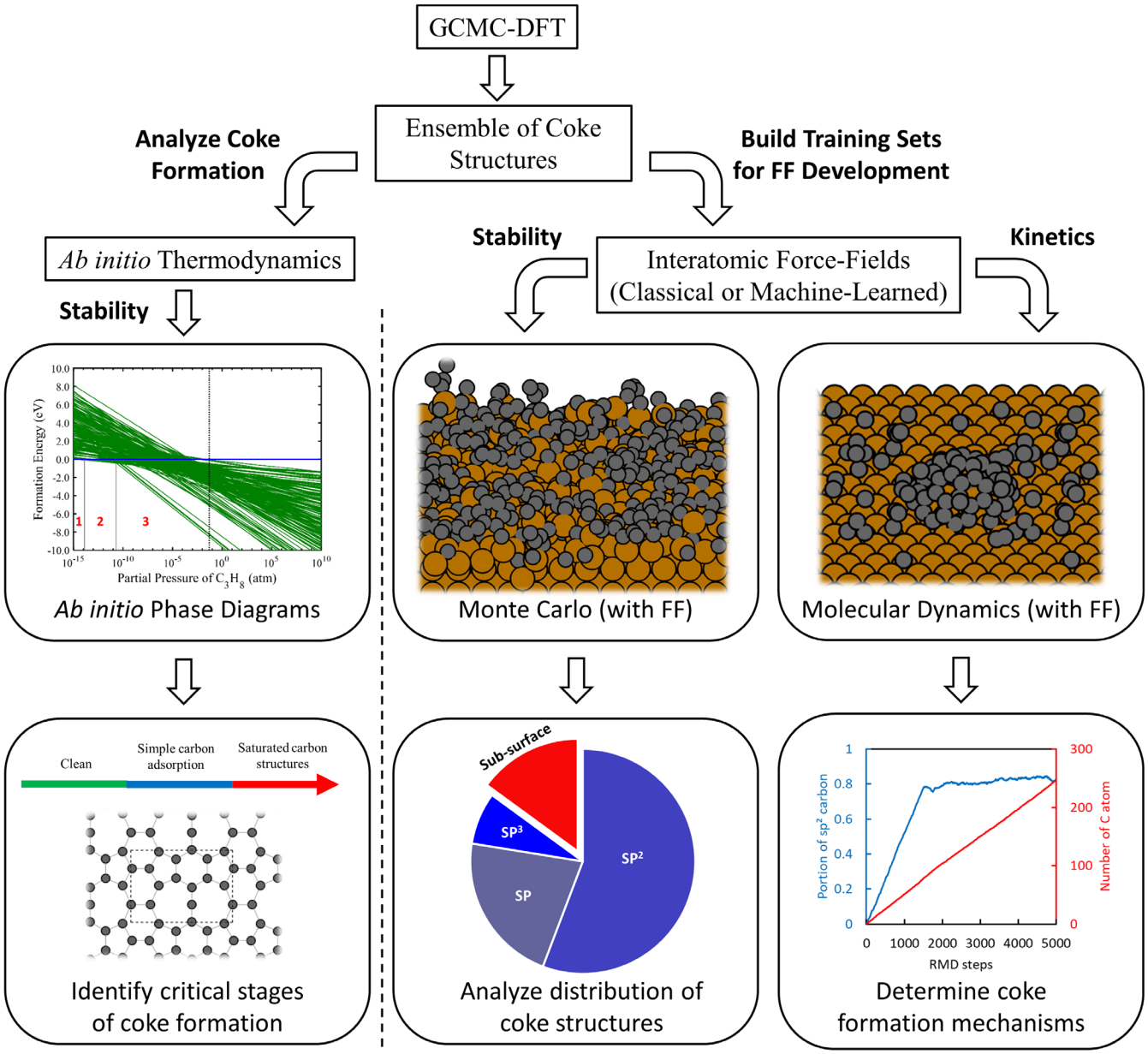

FIGURE 1 Concept for using grand canonical Monte Carlo (GCMC) simulations driven by density functional theory (DFT) and classical force fields, in conjunction with ab initio thermodynamics and molecular dynamics, to study coke formation on catalyst surfaces

2 | GCMC METHOD

GCMC is an effective sampling tool for generating structures automatically that lie at the stability phase boundary near conditions of interest. Here, we apply GCMC to simulate coke formation by introducing carbon atoms from a theoretical reservoir at a constant chemical potential of carbon. In each MC step, a carbon atom is either removed from the system and placed back in the reservoir, inserted into the system from the reservoir, or displaced within the system. Once the MC move is executed, the energy of the system is evaluated with the DFT settings described in section 1 of the Supporting Information. Using the new system energy, the move is accepted or rejected based on the following well-established[19] acceptance criteria:

$$P_{\text{remove}}^{\text{accept}} = \min\left[1, \frac{\Lambda^3 N}{V}\exp[-\beta(E_2 - E_1 + \mu_{\text{res}})]\right] \quad (1)$$

$$P_{\text{insert}}^{\text{accept}} = \min\left[1, \frac{V}{\Lambda^3(N+1)}\exp[-\beta(E_2 - E_1 - \mu_{\text{res}})]\right] \quad (2)$$

$$P_{\text{displace}}^{\text{accept}} = \min[1, \exp[-\beta(E_2 - E_1)]] \quad (3)$$

where P^{accept} is the calculated acceptance probability for each move type, Λ is the thermal de Broglie wavelength of the inserted/removed carbon atom, N is the number of carbon atoms in the system (before the MC step is executed), V is the volume of the system accessible to carbon atoms, β is the Boltzmann factor (i.e., $1/k_bT$), E_1 and E_2 are the energy of the system before and after the MC step, and μ_{res} is the specified chemical potential of the carbon reservoir.

The chemical potential of carbon was determined by the free energy of C_3H_8 and H_2, which are the dominant gas phase species during PDH. An environment at 873.15 K, 10^{-2} atm H_2, and 5×10^{-2} atm C_3H_8 was taken to be a representative PDH reaction condition.[44] We fixed the pressure of H_2 at 0.01 atm for all simulations. We conducted GCMC simulations at three C_3H_8 pressures of 5×10^{-5} atm, 5×10^{-2} atm, and 5×10 atm to sample relevant structures at carbon chemical potentials slightly above and below the PDH reaction condition. Furthermore, three independent GCMC simulations with different random number seeds were performed at each condition to ensure effective sampling.

The GCMC-DFT algorithm was implemented with an in-house Fortran code, where Unix system calls were used to launch the VASP 5.4.4 software to evaluate system energies. Our code is available via open-source license at (https://github.com/tsenftle/Coking-GCMC) (excluding access to VASP executables, which require a separate license issued by VASP Software GmbH). An overview of the algorithm is shown in Figure 2. The simulation begins by selecting an MC move to execute on the initial surface structure, where a random number generator is used to ensure that move types are selected with even frequency. The code can remove a random carbon atom, displace a random carbon atom, or add a carbon atom at a random set of coordinates. We constrained the random coordinates for insertion to be within 3 Å of the surface and at least 1.4 Å away from the nearest existing atom in the system. These settings prevent the algorithm from sampling highly unfavorable structures. All random coordinates for inserted carbon atoms are constrained to the region above the surface to avoid high-energy structures caused by carbon insertion in the subsurface region. Thus, this study only considers coke formation on the surface and neglects carbide formation in the subsurface region. The geometry of the new system structure after the MC move then is relaxed with the DFT settings described in Supporting Information section 1. The acceptance probability of the move is calculated with Equations (1)–(3), which is enforced by drawing a random number between zero and one to determine whether or not the MC move is accepted. The simulation then enters the loop again to start another random move.

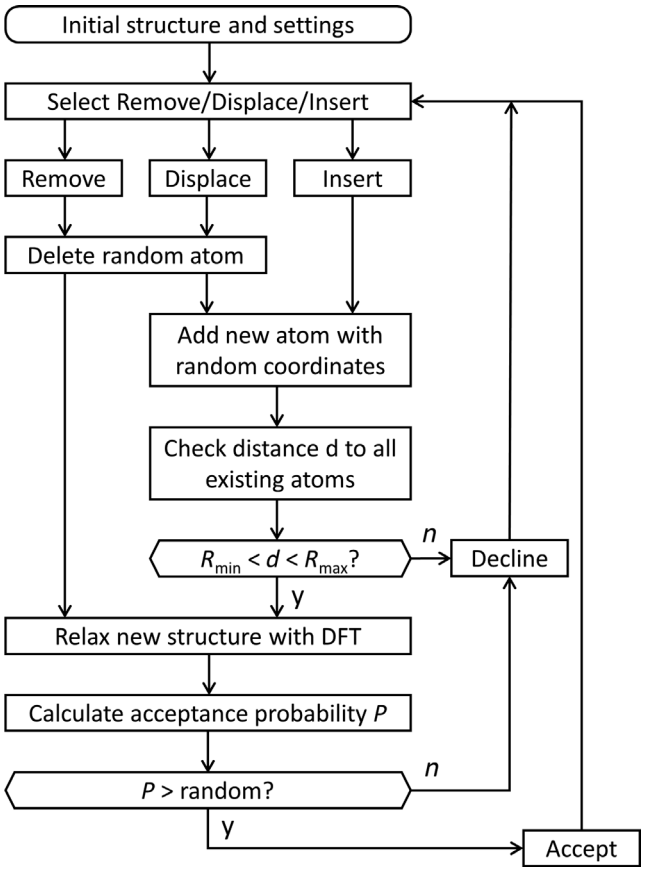

FIGURE 2 Schematic of the grand canonical Monte Carlo-density functional theory (GCMC-DFT) algorithm

Due to the high computational cost of DFT, we introduced a forward bias to accelerate the exploration of stable surface states and to minimize consideration of unstable structures. First, insertion and displacement moves that draw random coordinates outside of the maximum distance from the surface or within the minimum distance to another atom (defined above) are directly declined, so no computational resources are wasted evaluating the energy of structures that will be highly unstable. Second, after each MC move the algorithm executes a structural relaxation step that brings the system into its nearest local minimum. Single-point calculations at randomly generated positions would result in a low acceptance rate that is computationally intractable. The forward biases affect the ensemble statistics

of the resulting structures, so here we did not derive any physical quantities from such statistics. Furthermore, we evaluated the relative stability of all resulting structures using the formalism of ab initio thermodynamics, and thus we assessed whether or not a structure appearing in the ensemble of geometries is stable under a given set of reaction conditions. The GCMC method employed here serves simply as a tool for more effectively sampling the most relevant region of the phase diagram without a priori knowledge of surface structures.

3 | RESULTS AND DISCUSSION

3.1 | Coke formation on Fe(110)

We first investigated coke formation on metallic iron with the GCMC tool set to establish a baseline understanding of unrestricted coking processes on carbophilic surfaces. We analyzed all the coke structures on the Fe(110) surface sampled in accepted moves of the GCMC simulations with the ab initio thermodynamics formalism. By assuming those structures are in equilibrium with gas phase, the free energy of carbon atoms can be computed with ab initio thermodynamics, which is described in detail in section 3 of the Supporting Information. The free energy of each carbon-adsorbed surface computed relative to the clean surface is plotted in Figure 3 as a function of varying C_3H_8 pressure (i.e., as a function of varying chemical potential of carbon as given by the equations in section 3 of the Supporting Information at fixed $T = 873.15$ K and $P_{H2} = 10^{-2}$ atm). The formation energies are linear functions of the chemical potential of carbon with the slope determined by the number of carbon atoms inserted into the system. The typical reaction condition of PDH (i.e., 5×10^{-2} atm propane) is marked with a dotted vertical line. It is clear that, even at low propane pressure (10^{-15} atm), some structures have negative formation energies indicating the onset of carbon adsorption. Almost all of the structures sampled by the GCMC algorithm are more stable than the clean

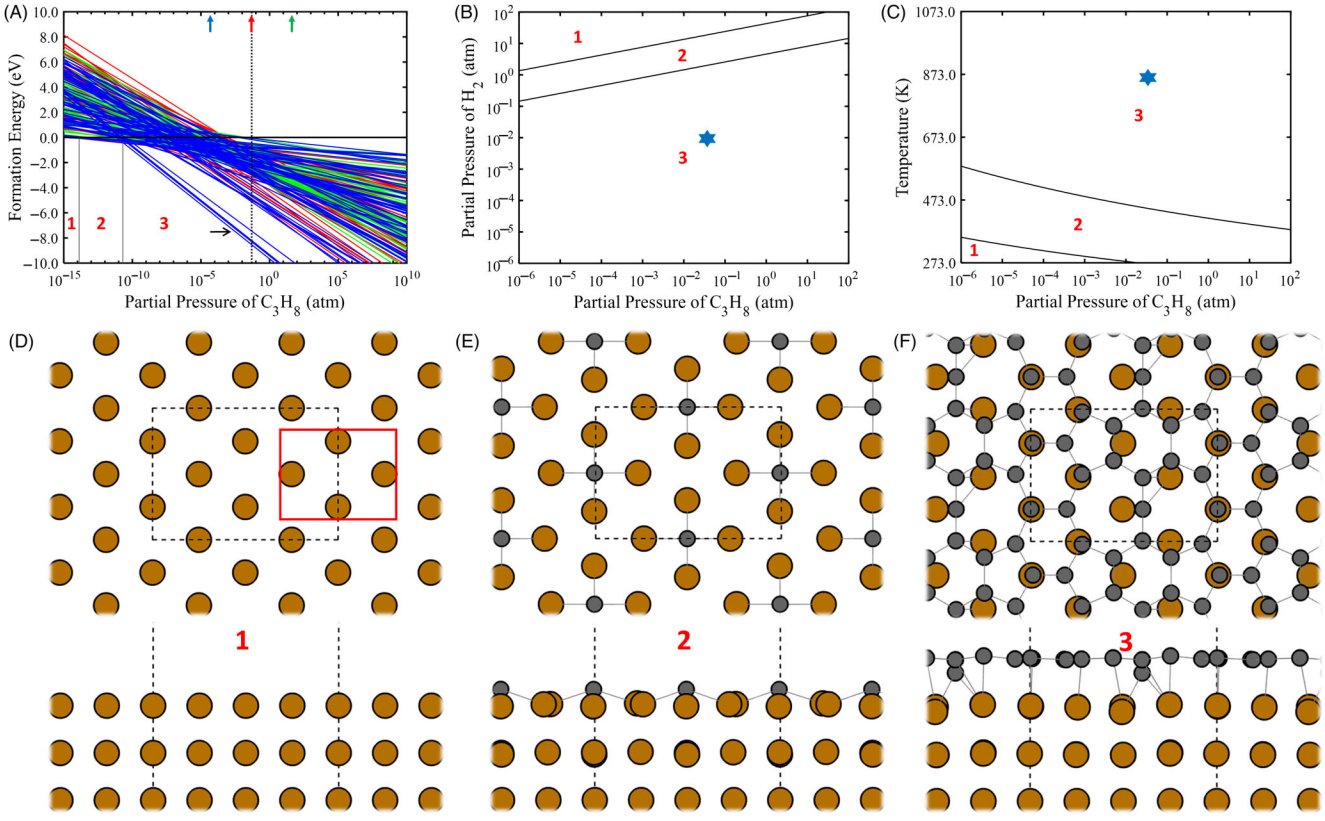

FIGURE 3 (A) Phase diagram of surface coke formation on Fe(110) with structures generated by grand canonical Monte Carlo (GCMC) at C_3H_8 pressures of 5×10^{-5} atm (blue), 5×10^{-2} atm (red), and 5×10 atm (green). The x axis is the partial pressure of propane in log-scale and the temperature is 873.15 K and H_2 pressure is 10^{-2} atm. The black vertical dotted line is the typical reaction condition for propane dehydrogenation (PDH) where the propane pressure is 5×10^{-2} atm. The y axis is the formation energy of each structure relative to that of the clean surface (blue horizontal line). The phase diagram is delimited to three zones demarking different lowest-energy structures, labeled with red numbers 1, 2, and 3. (B) The phase diagram of the most stable structures at varying pressures of both C_3H_8 and H_2 at fixed $T = 873.15$ K. Black lines represent the phase boundary. The typical reaction condition for PDH is marked with a blue star. (C) The phase diagram of the most stable structures at varying temperature and pressure of C_3H_8 at fixed 0.01 atm H_2. Black lines represent the phase boundary. The typical reaction condition for PDH is marked with a blue star. The following panels show the top view (top) and side view (bottom) of the most stable structures identified from the phase diagram at (D) region 1 (pristine surface), (E) region 2, and (F) region 3. Fe is brown, C is gray. The unit cell is shown with black dashed lines. The identified stable adsorption site for a single carbon atom is marked on the pristine surface with a red box

surface at 0.05 atm of propane, demonstrating the high thermodynamic stability of adsorbed coke under PDH reaction conditions. In the 2D phase diagrams of Figure 3B,C, the marked PDH reaction condition is far from the phase boundary between phases 2 and 3, suggesting that the coke structure in phase 3 with 15 carbon atoms on Fe(110) is highly stable at the reaction condition. Thus, the simulations predict that pure iron will rapidly coke and deactivate during PDH, which is in agreement with the runaway coking observed in experiment.[44]

We examine more closely the stable coke structures formed on Fe(110) by dividing the phase diagram in Figure 3A into three regions that each have a different lowest-energy structure (labeled as regions 1, 2, and 3). Figure 3D corresponds to a pristine Fe(110) surface, which is most stable at a very low chemical potentials of carbon. As μ_C increases, the adsorption of single carbon atoms becomes favorable, where the most stable structure in region 2 has two carbon atoms occupying hollow sites on the surface (Figure 3E). A large jump in the number of carbon atoms on the surface occurs in region 3, where a network of 15 carbon atoms forms with high thermodynamic stability. This structure consists of a continuous carbon sheet covering the entire surface, where 14 out of the 15 carbon atoms achieve a stable sp^2 configuration. Thus, graphite-like coke structures are prevalent on Fe surfaces, which is in agreement with experimental observations. For instance, Wrobel et al.[69] observed that iron particles are covered by thin 2D carbon layers in methane/hydrogen environments. Zhang et al.[70] also observed the formation of Fe particles with 2D carbon layers in floating catalyst chemical vapor deposition experiments. Conversely, graphitic carbon is less favored on Pt surfaces. Using pyrolysis GC–MS, Wang et al.[45] identified aliphatic, aromatic, and pre-graphite coke structures on Pt-Sn/Al_2O_3 catalysts during PDH. Pre-graphite carbon only contributed to 26.6% of the coke structure, while aliphatic carbon accounted for 69.0%.

In region 3 of Figure 3A, there are several structures with superior stability compared to the majority of the other structures in this region (marked with a black arrow). We analyze the stepwise development of the stable, saturated 2D planar coke structure (Figure 3D) to understand why there is a sudden increase in the stability of this particular structure. Figure 4A describes the change of formation energy and C atom number versus the MC steps. Based on the formation energies, three sequential growth stages are identified: carbon atom adsorption and accumulation, carbon ring formation, and 2D carbon network formation. The key structure at the transition points are marked with a black arrow and their geometries are shown in Figure 4. At the carbon accumulation stage, carbon atoms are deposited onto the surface and form simple carbon structures, such as carbon dimers and simple chains (Figure 4B,C). A significant drop in the formation energy occurs when there is enough carbon to form ring structures, as shown in the comparison of Figure 4C,D. In the final stage, the coke structure gains high stability as it completes a 2D network with all carbon bonds saturated. The new carbon atom added in structures that undergo a large drop in the formation energy is marked with a red circle. In the final stages, the added carbon completes the 2D bonding structure by saturating carbon atoms that were in a sp^1 configuration (blue arrows in the figure). This induces a significant drop in the formation energy of the entire configuration (by over 2 eV), thus creating the gap between structures seen in Figure 3A. As shown in Figure 4G, the most stable structure is formed by the addition of a carbon atom that bonds with three different sp^1 carbons to form sp^2 configurations. The increase in sp^2 carbon is responsible for the increased stability of the coke structure, which implies that geometric effects can prevent coke formation by stopping the formation of planar carbon networks with saturated sp^2 bonding (i.e., by isolating carbon adsorption sites). These findings also can provide insight for carbon-nanotube (CNT) formation. For instance, Zhang et al.[70] found that planar carbon layers are formed on Fe surfaces in the absence of sulfur, whereas abundant CNTs are formed in the presence of sulfur. When the formation of 2D planar structures is disrupted by surface modifiers, such as sulfur, the only way to saturate carbon bonding is the formation of carbon caps that then lift from the surface through CNT growth.

3.2 | Coke formation on iron carbide, iron sulfide, and Fe/Al alloys

Pure iron is known to suffer from runaway coking under PDH[44,60] conditions, while other Fe-based materials, such as Fe_3C[44] and FeS,[50,51] have shown high coke resistance. Here, we perform GCMC and ab initio thermodynamics analyses to better understand why these materials are resistant to coke formation. We also study an Al/Fe alloy, $Al_{13}Fe_4$, that was found to be stable for the semi-hydrogenation of acetylene[64] and hydrogenation of butadiene,[65] but has not yet been tested for PDH (to our knowledge). We also tested another alloy, FeAl,[66] so that we can assess the role composition plays in determining coke formation over Al/Fe alloys.

Figure 5A shows the phase diagram of coke formation on Fe_3C (010). At the reaction condition indicated by the black vertical dashed line, most coking structures are less stable than the pristine surface, suggesting that this surface has relatively high resistance to coking. Only one structure containing three adsorbed carbon atoms is found to be stable under reaction conditions. This structure is stable because the adsorbed carbon atoms from the gas phase (shown in gray in Figure 5E) form a 5-carbon chain with two carbon atoms from the Fe_3C lattice (shown in black in Figure 5E). However, this structure's relative formation energy is close to zero (−0.2 eV), indicating that the adsorbed carbon atoms can be easily removed from the surface. The typical reaction condition marked with a blue star is located in region 2 and is far from the boundary of phase 3 where carbon chains begin to form, suggesting that this surface will be resistant to coke formation. Another structure with six adsorbed carbon atoms is stable at 10^7 atm C_3H_8 partial pressure, as shown in Figure 5F. Two carbon atoms are adsorbed above different lattice carbon atoms, forming surface dimers. The remaining four carbon atoms form a carbon chain that lies in a relatively high position above the surface. This implies that carbon may prefer to form filaments lifting off of Fe_3C surfaces rather than the planar 2D structures observed on pure iron. Another distinction between Fe_3C and Fe is that there is no stable state

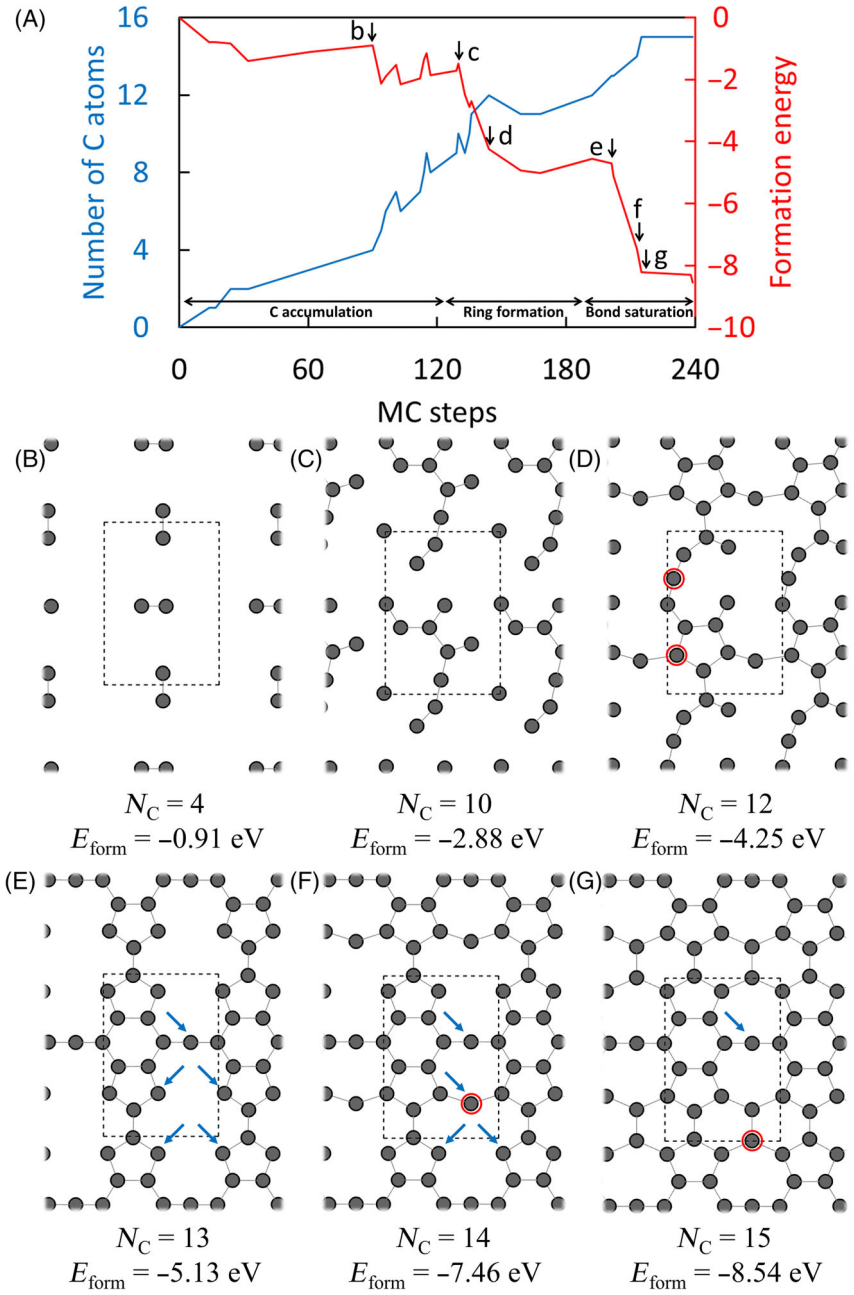

FIGURE 4 (A) The number of C atoms (blue) and formation energy (red) with Monte Carlo (MC) steps in the grand canonical MC (GCMC) simulation on Fe(110). The formation energy is referenced to a clean surface and a gas phase of 0.05 atm C_3H_8 and 0.01 atm H_2 at 600°C. Key carbon structures, marked by arrows in panel (A), are shown in panels (B–G). C atoms are gray, and all Fe atoms are omitted for clarity. One unit cell is shown with black dashed lines. The corresponding numbers of carbon (N_C) and formation energies at the propane dehydrogenation (PDH) condition (E_{form}) are included under each panel

involving a single carbon atom on the Fe_3C surface, suggesting that the nucleation of coke structures via single atoms is not favorable. These results also confirm the inherent high coke resistance of Fe_3C. We calculated the free energy of Fe_3C relative to Fe as a function of the reaction conditions with ab initio thermodynamics as shown in Figure S2. It follows the same formalism in eq. 1 of the Supporting Information but uses the energy of bulk structures. Fe_3C is shown to be much more stable than Fe under the typical PDH reaction condition as indicated by the vertical dotted line. However, in the experiments of Tan and coworkers, they found that the addition of phosphate is necessary to form Fe_3C from Fe in PDH environment by stopping rapid coke formation which prevents the phase transition.[44] Otherwise the runaway coking on Fe kinetically prevents the phase transition and deactivates the catalysts, which agrees with our results showing that carbon overlayers are highly stable on Fe(110). In the experiments, it was unclear whether Fe_3C was coke-resistant or the phosphate in the catalysts was necessary to maintain stability against coking. Our results in this work suggest that a preformed iron carbide will also show high coke resistance in PDH.

The FeS(001) surface is highly resistant to coking, and as such no carbon was deposited on the surface after several attempted GCMC insertions. All attempted insertion moves were rejected because there is no stable adsorption site for a carbon atom on the FeS(001) surface. Thus, we include the analysis of the energies and most stable structures in section 5 of the Supporting Information.

Next, we examine coke formation on an FeAl alloy, which was chosen because of its structural similarity to pure Fe. The FeAl(110) surface has the same surface geometry as the Fe(110) surface in

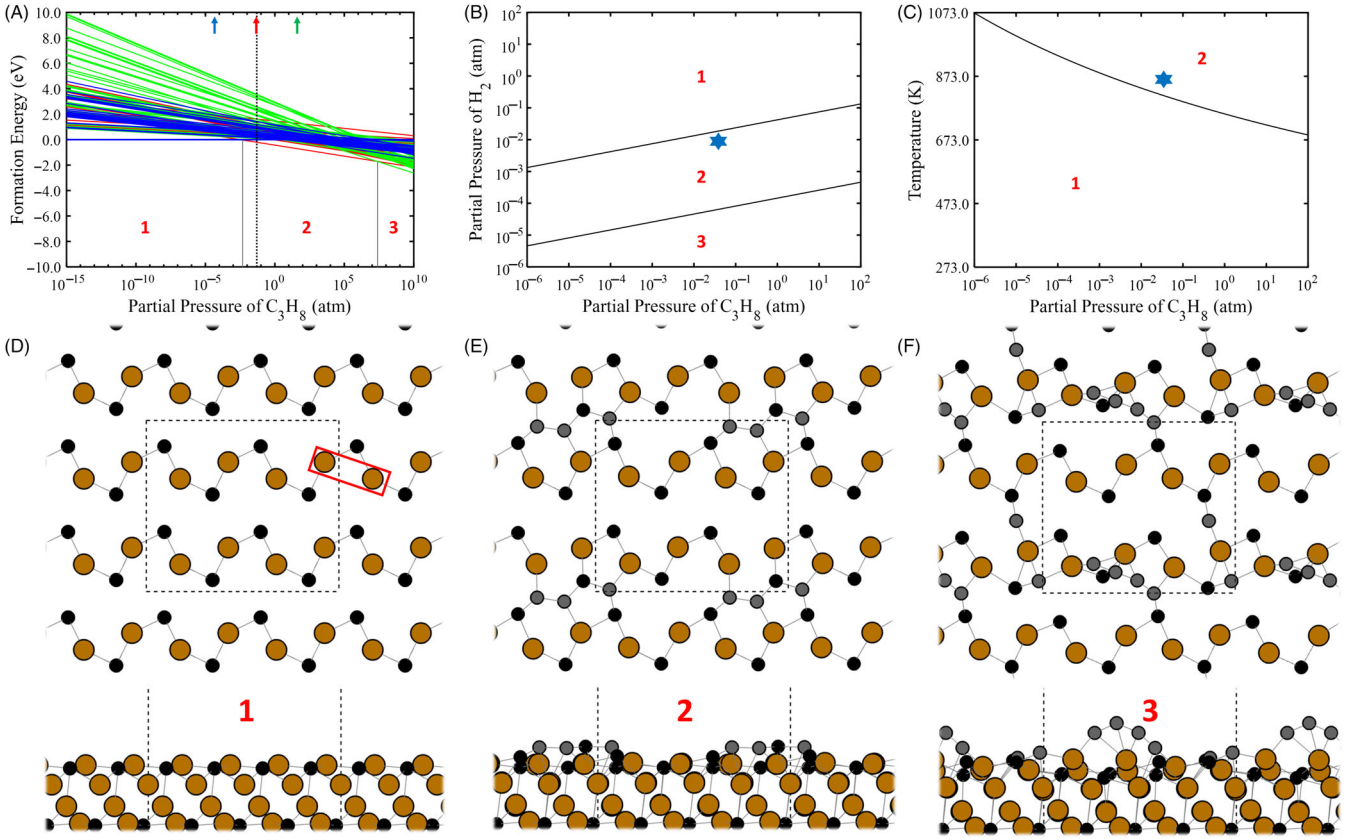

FIGURE 5 (A) Phase diagram of surface coke formation on $Fe_3C(010)$ with structures generated by grand canonical Monte Carlo (GCMC) at C_3H_8 pressures of 5×10^{-5} atm (blue), 5×10^{-2} atm (red), and 5×10 atm (green). (B) The phase diagram of the most stable structures at varying pressures of both C_3H_8 and H_2 at fixed $T = 873.15$ K. Black lines represent the phase boundary. The typical reaction condition for propane dehydrogenation (PDH) is marked with a blue star. (C) The phase diagram of the most stable structures at varying temperature and pressure of C_3H_8 at fixed 0.01 atm H_2. Black lines represent the phase boundary. The typical reaction condition for PDH is marked with a blue star. The following panels show the top view (top) and side view (bottom) of the most stable structures identified from the phase diagram at (D) region 1, (E) region 2, and (F) region 3. Only the topmost layer of the surface is shown in the top view in each panel. The carbon atoms inserted by GCMC are gray and the carbons from the carbide surface are black

terms of atom positions, but with a row of Fe atoms substituted by Al atoms (Figure 6D). The GCMC simulation reveals four stages in the coke formation process on the FeAl(110) surface as the carbon chemical potential increases (Figure 6A). Region 1 of the phase diagram consists of the clean surface, which is stable at propane pressures below $\sim 10^{-13}$ atm. In regions 2 and 3 of the phase diagram, single carbon atoms at the Fe—Fe bridge sites are stable with 50% and 100% site occupancy, respectively (Figure 6E,F). Carbon atom adsorption occurs on the Fe—Fe bridge sites, demonstrating that carbon adsorption is more favorable on Fe than on Al. (The influence Al on the electronic structure of Fe and its effect on C adsorption will be discussed in more detail in the next section.) In region 4, a carbon structure with a network of 16 carbon atoms is found to be stable over a large pressure range (Figure 6G). On the 2D phase diagrams the typical reaction is located to region 4 and is far from the phase boundary, suggesting this structure is stable in a large range of reaction conditions. Although this carbon network structure is different from the one that forms on the Fe(110) surface (Figure 3F), it still features many sp^2 carbon configurations leading to a significant drop in the formation energy. However, because of the less stable Al—C bond compared to the Fe—C bond, the formation energy of the most stable structure on this surface is −5.76 eV, compared to −8.54 eV on the Fe(110) surface. Thus, coke may still form on the FeAl(110) surface during PDH, but it will be less stable than the coke formed on the Fe(110) surface.

We tested another alloy, $Al_{13}Fe_4$, to better understand how coke formation is affected by a higher ratio of the Al to Fe. The resulting phase diagram for $Al_{13}Fe_4(010)$ is shown in Figure 7A. On this surface, all Fe atoms on this surface are isolated by Al pentagons (marked by green lines in Figure 7D). As a result, no Fe—Fe bridge sites are present and the adsorption of a single carbon atom instead occurs at a fourfold Al hollow site, which is found to be stable at very low propane pressures (Figure 7E). Structures with more carbon start to become stable at pressures comparable to those observed on the Fe_3C surface, suggesting that $Al_{13}Fe_4$ may have similar coke resistance to Fe_3C during PDH. However, the coke structures on $Al_{13}Fe_4$ differ from those observed on both Fe and Fe_3C. The stable structures appearing in regions 3 and 4 of the phase diagram are not carbon chains or complex carbon networks but rather are carbon single atoms

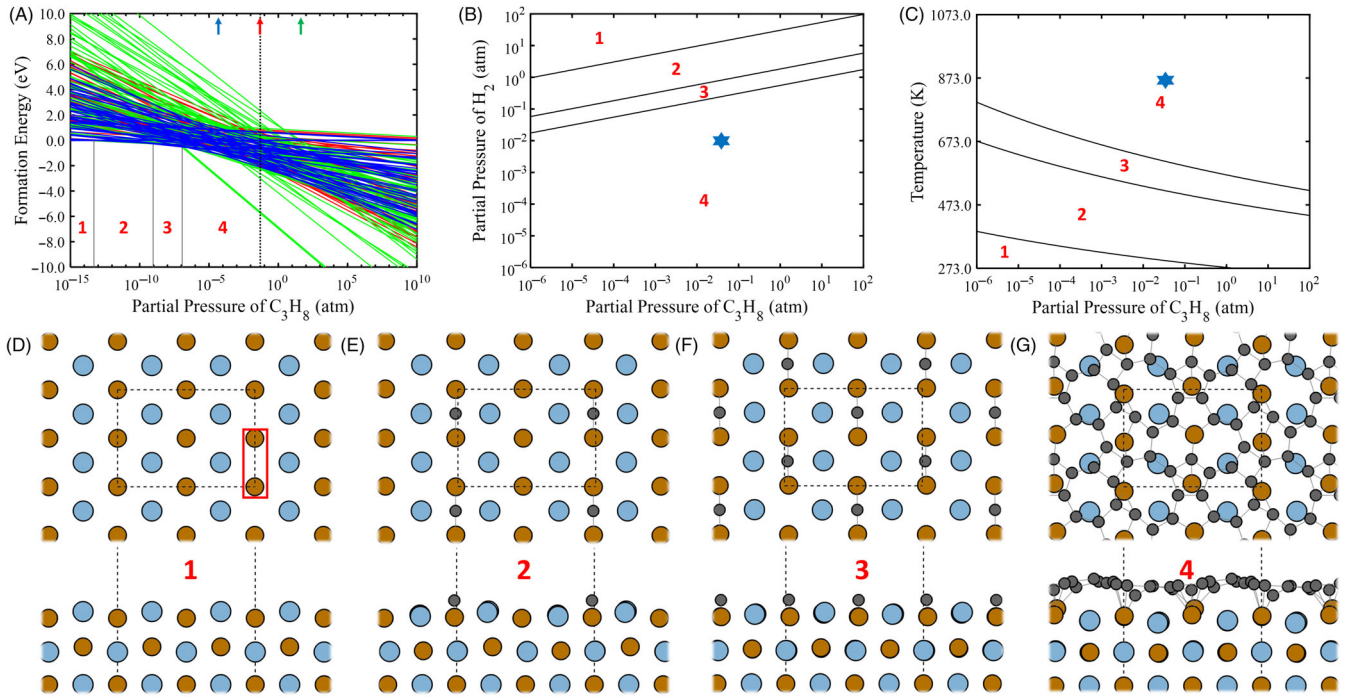

FIGURE 6 (A) Phase diagram of surface coke formation on FeAl(110) with structures generated by grand canonical Monte Carlo (GCMC) at C_3H_8 pressures of 5×10^{-5} atm (blue), 5×10^{-2} atm (red), and 5×10 atm (green). (B) The phase diagram of the most stable structures at varying pressures of both C_3H_8 and H_2 at fixed $T = 873.15$ K. Black lines represent the phase boundary. The typical reaction condition for propane dehydrogenation (PDH) is marked with a blue star. (C) The phase diagram of the most stable structures at varying temperature and pressure of C_3H_8 at fixed 0.01 atm H_2. Black lines represent the phase boundary. The typical reaction condition for PDH is marked with a blue star. The following panels show the top view (top) and side view (bottom) of the most stable structures identified from the phase diagram at (D) region 1, (E) region 2, (F) region 3, and (G) region 4

or carbon dimers (Figure 7F,G). Although Al sites are less favorable for carbon adsorption, carbon adsorption still occurs on Al—Al bridge and hollow sites because all Fe atoms are isolated. The lack of Fe—Fe sites and high coverage of Al atoms prevents the formation of both carbon chains and 2D carbon networks.

3.3 | Mechanisms for coke resistance

We calculated the expected coverage of the surface structures with a Boltzmann distribution, as shown in Figure S3. For each surface, the coverage is dominated by the most stable structure. For Fe(110) the most stable 2D carbon network dominates 95% of the surface, while two other coking structures (both with 15 carbon atoms in the cell) represent 5% of the surface. Therefore, the Fe(110) surface will be totally covered by carbon overlayers. Similarly, on FeAl(110) the distribution is dominated by two coking structures with 16 carbon atoms in the cell. On Fe_3C(010), as the formation energies of various carbon adsorption structures are close, there are many structures that contribute to the surface coverage. The most stable structure with three carbon atoms dominates the surface coverage at 85%. The clean surface also covers 5% of the surface, suggesting that Fe_3C(010) has relatively high coke resistance and will expose clean surface sites to the reaction environment. For FeS(001), the pristine surface dominates 100% of the surface since no carbon adsorption is stable.

We further analyzed the electronic structure of each surface to understand the dominant effect (e.g., electronic effect or geometric effect) for the different levels of coke resistance in each surface. It has been widely observed that electron-withdrawing groups increase the coke resistance of iron catalysts in carbon-rich environments. For instance, Sun et al.[46,47,61] found that adding sulfate during synthesis or cofeeding SO_2 with reactants can stabilize Fe-based catalysts during PDH. Tan et al.[44] found that the addition of phosphate in the preparation of Fe catalysts suppresses coke formation, while still permitting the bulk phase transformation to form iron carbide under reaction conditions. Furthermore, in our previous work,[63] we used crystal orbital Hamilton population (COHP) analyses to demonstrate that coadsorption of a PO_4 group on the Fe(110) surface drains d-state electrons from surface Fe and thus weakens carbon binding on the surface.

We first analyzed the Bader charge[71] of Fe atoms on each surface to determine if similar effects are at play on the surfaces studied herein. Here, we define "surface Fe atoms" to mean all Fe atoms with z positions within 1 Å of that of the topmost Fe atom. The average Bader charge of surface Fe atoms in each system is summarized in Table 1. For each surface, the single carbon formation energy is the formation energy of the most stable structure with one C atom. The

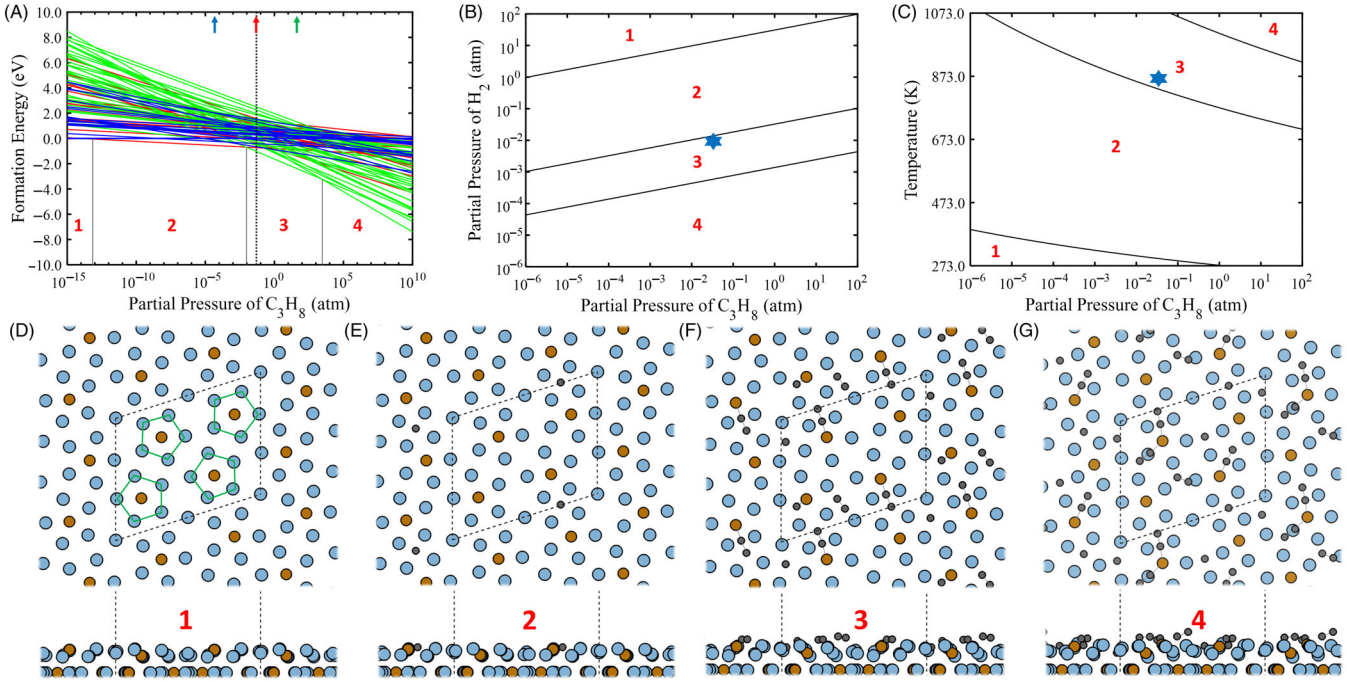

FIGURE 7 (A) Phase diagram of surface coke formation on $Al_{13}Fe_4(010)$ with structures generated by grand canonical Monte Carlo (GCMC) at C_3H_8 pressures of 5×10^{-5} atm (blue), 5×10^{-2} atm (red), and 5×10 atm (green). (B) The phase diagram of the most stable structures at varying pressures of both C_3H_8 and H_2 at fixed $T = 873.15$ K. Black lines represent the phase boundary. The typical reaction condition for propane dehydrogenation (PDH) is marked with a blue star. (C) The phase diagram of the most stable structures at varying temperature and pressure of C_3H_8 at fixed 0.01 atm H_2. Black lines represent the phase boundary. The typical reaction condition for PDH is marked with a blue star. The following panels show the top view (top) and side view (bottom) of the most stable structures identified in (D) region 1, (E) region 2, (F) region 3, and (G) region 4. Al is light blue, Fe is brown, and C is gray. The single Fe atoms surrounded by a pentagon of Al atoms is highlighted with green lines in panel (B)

lowest formation energy is the formation energy of the most stable structure with any number of C atoms among all sampled structures. The Bader charge of surface Fe atoms on Fe_3C and FeS are $+0.56e$ and $+0.76e$, respectively, indicating a large charge transfer due to the electron-withdrawing effect from either C or S (e is the positive elementary charge). The amount of charge transfer trends with the degree of destabilization experienced by the single adsorbed carbon atom (measured by the change in adsorption energy). We also performed a density of states (DOS) and d-band center analyses for the surface Fe atoms. The projected DOS of d-state electrons for Fe on each surface, as well as that of the valence electrons of all surface Al atoms, are shown in Figure 8. The d-band center of the surface Fe atoms are summarized in Table 1. The formation energy of the most stable coke configuration identified by GCMC under PDH conditions is also included in Table 1, from which the relative coke resistance is determined. The DOS summarizing the d-state electrons of the Fe_3C (010) surface (Figure 8B) and the FeS(001) surface (Figure 8C) retain a shape profile that is similar to that of metallic iron, but with a clear shift to lower energy compared to the Fe(110) surface (Figure 8A). As a result, the d-band center of the $Fe_3C(010)$ and FeS(001) surfaces are -1.36 eV and -1.58 eV, respectively, which are both much lower than that of Fe(110) at -0.97 eV. The difference in d-band center is caused by the electron-withdrawing effect from either carbon or sulfur, since the Bader charge of surface Fe atoms is $-0.01e$, $+0.56e$, and $+0.76e$ for Fe(110), $Fe_3C(010)$, and FeS(001), respectively. The carbon binding is weakened by depleted charge in Fe—C bonding

TABLE 1 Comparison of Bader charge, d-band center, and coking resistance of each surface

Surface	Bader charge (e)	d-band center (eV)	Single carbon formation energy (eV)	Lowest formation energy (eV)	Coking resistance
Fe(110)	−0.01	−0.97	−0.80	−8.54	Low
$Fe_3C(010)$	+0.56	−1.36	0.10	−0.21	High
FeS(001)	+0.76	−1.62	1.24	1.24	Very high
FeAl(110)	−1.07	−1.40	−0.73	−5.76	Moderate
$Al_{13}Fe_4(010)$	−2.91	−0.97	0.35	−1.04	High

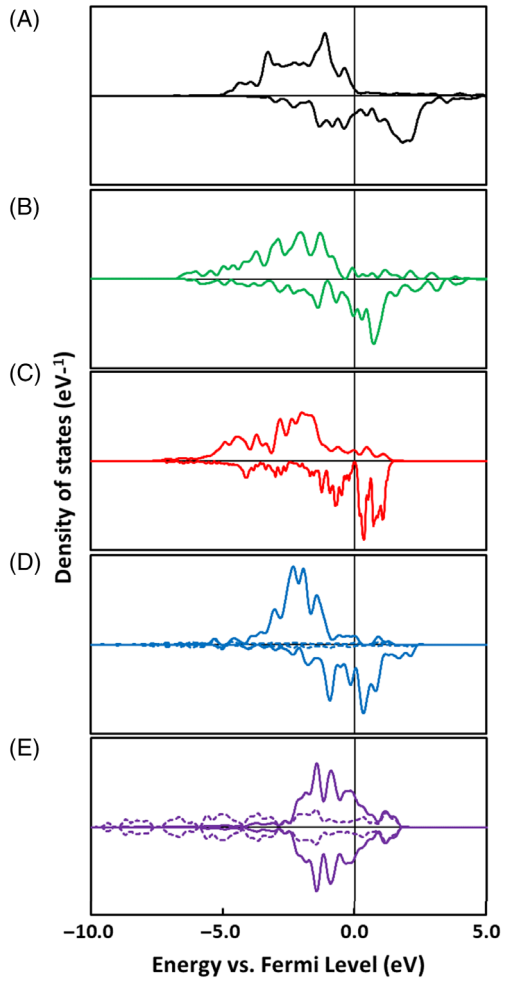

FIGURE 8 Spin-polarized projected density of states of (A) Fe(110), (B) Fe_3C(010), (C) FeS(001), (D) FeAl(110), and (E) $Al_{13}Fe_4$(010). Solid lines are the d-states of surface Fe atoms. Dashed lines are the valence electrons of Al in the FeAl and $Al_{13}Fe_4$ surfaces

states; thus, the carbon binding energy correlates with the Bader charge and d-band center position. However, these trends do not follow for Fe—Al alloy surfaces because Al donates electrons to Fe, as the Bader charge of surface Fe is −1.07e for FeAl(110) and −2.91e for $Al_{13}Fe_4$(010). In this case, surface carbon is destabilized by the population of Fe—C anti-bonding states, which is described in detail in the following section. Thus, electronic effects readily account for the increased coking resistance observed for both Fe_3C and FeS, whereby charge depletion from the Fe d-states leads to less stable C adsorption, in agreement with our previous work showing similar effects when electron-withdrawing groups are introduced on the Fe(110) surface.[63]

On the other hand, the direction of charge transfer and the shift in the position of the d-band center does not account for the coke resistance characteristics of the Fe/Al alloys. Al atoms donate electrons to Fe on both alloy surfaces, and the more negatively charged Fe atoms do not exhibit stronger Fe—C bonding. FeAl(110) has a similar d-band center position compared to the Fe_3C(010) surface, yet on the FeAl(110) surface 2D coke structures are stable. $Al_{13}Fe_4$(010) has almost the same d-band center as Fe(110), but displays much higher coking resistance. To understand these effects, we performed COHP analysis for the single carbon adsorption on metallic iron and compared it to that of the Fe/Al alloys (Figure 9). The upper half of the figure shows the top view of each single carbon adsorption configurations, where black arrows indicate the Fe—C bonds analyzed in the lower half by plotting the COHP interaction between the d-states of Fe and p-states of C. The x axis plots the negative partial COHP (−pCOHP), so the right side indicates bonding states and left side indicates anti-bonding states. As shown in Figure 9BC, the extra electrons donated by Al to Fe populate Fe—C anti-bonding states (indicated by red arrows) near the Fermi-level. This effect is especially pronounced for the $Al_{13}Fe_4$(010) surface, explaining why even single C atom adsorption on the Fe site is not favorable (Figure 9C). Thus, electron-donating groups can also destabilize adsorbed carbon.

Both electronic and geometric effects are at play in the Fe/Al alloys. On FeAl(110), although large Fe ensembles are disrupted by Al, there are still many Fe—Fe bridge sites rich in electron density that are available to provide favorable sites for carbon adsorption. The linear nature of the Fe rows leads to the formation of simple carbon chains that are dominated by sp^1 configurations at lower carbon chemical potentials. While carbon deposits can form on FeAl(110), they are much less stable than the planar sp^2 carbon networks that form on the pure Fe(110) surface. The $Al_{13}Fe_4$(010) surface exhibits the strongest geometric effect, as all Fe atoms are isolated by surrounding Al atoms. Single carbon atoms favorably adsorb on Al hollow sites, but complex carbon networks and chains are not stable on this surface.

Here, we assume that carbon will displace adsorbed hydrogen under carbon-rich conditions, so no explicit hydrogen was included in the GCMC analysis. We validated this assumption with test GCMC simulations that allow both carbon and hydrogen to be added to the system (with the chemical potential of hydrogen computed from the PDH condition at 600°C, 0.01 atm H_2, and 0.05 atm C_3H_8). These simulations generate surface formations that contain both C and H on the surface. When we compare the formation energy of these surfaces (with hydrogen and carbon chemical potentials referenced to 0.01 atm H_2 and 0.05 C_3H_8 at 600°C), we find that surfaces containing only adsorbed carbon are always more stable near the PDH reaction conditions, which is evident in Figure S4. As seen in the figure, some C_xH_y structures (shown in red) are relevant at very low carbon potential, but the surface will be dominated by carbon-only structures (shown in blue) at typical PDH conditions. Finally, we also initiated a GCMC simulation allowing hydrogen addition that started with the most stable, graphene-like carbon structure on the Fe(110) surface to determine if H could disrupt the carbon-rich structure. We found that few hydrogen insertion steps were accepted, and any inserted hydrogen was quickly removed (Figure S5). This agrees with the findings in Figure S4, showing that the carbon-only surfaces are most relevant at PDH conditions. Thus, the assumption that the surface is dominated by carbon is valid near the PDH conditions of

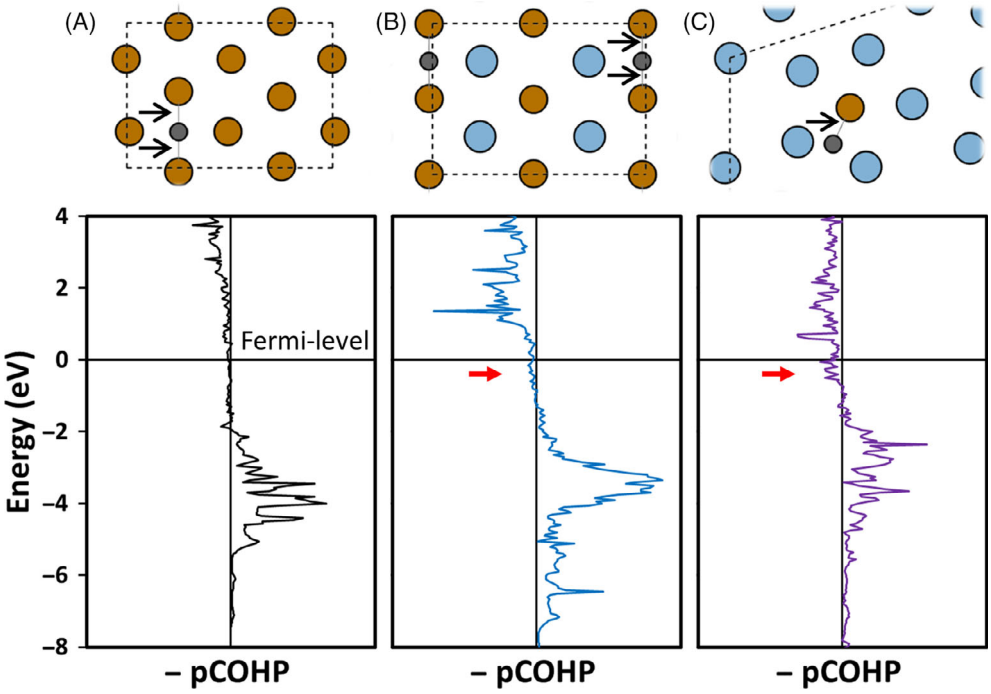

FIGURE 9 The top view of the single carbon adsorption configuration (up) and the corresponding COHP analysis (down) on (A) Fe(110), (B) FeAl (110), (C) $Al_{13}Fe_4$(010). The y axis is the energy referred to Fermi-level. The x axis is negative partial COHP (−pCOHP). Each COHP curve is the sum of the interaction between d-states of Fe with p-states of C in the Fe—C bonds indicated by black arrows in the geometry

interest in this paper. In general, hydrogen in the system will increase the coking resistance of the surface by disrupting the formation of stable carbon networks. Therefore, the simulations in this work represent an upper bound for coke formation.

4 | CONCLUSION

In this work, we developed a computational toolset for modeling phase formation on catalyst surfaces with GCMC and ab initio thermodynamics, which allows us to evaluate the phase formation process without any prior knowledge of the system's phase diagram. This toolset is applied to the study coke formation during PDH on Fe-based catalysts (i.e., Fe_3C, FeS, FeAl, and $Al_{13}Fe_4$). FeAl is predicted to have higher coking resistance than metallic iron but may still suffer from coke formation under carbon-rich environments. $Al_{13}Fe_4$ is predicted to have high resistance to coking in PDH environments. This study demonstrates that coking resistance can be achieved either by introducing electron-withdrawing or electron-donating groups to weaken the Fe—C bonding or by alloying Fe with less carbophilic elements to disrupt planar Fe ensembles that promote the formation of 2D carbon networks. Analysis of electronic structures shows that the Fe d-band in Fe_3C and FeS surfaces is shifted to lower energy by the electron-withdrawing constituents, which weakens adsorbed carbon. On Fe/Al alloys, Al donates electron density to Fe, which populates anti-bonding of Fe—C states near the Fermi-level and weakens carbon adsorption. Overall, we find that electronic effects induced by both electron-withdrawing and electron-donating constitutions can destabilize adsorbed carbon atoms, whereas geometric effects are important for preventing the formation of 2D carbon networks.

CONFLICT OF INTEREST

The authors declare no conflicts of interest.

DATA AVAILABILITY STATEMENT

The data that support the findings of this study are openly available in repository "Coking-GCMC" at https://github.com/tsenftle/Coking-GCMC.

ORCID

Thomas P. Senftle https://orcid.org/0000-0002-5889-5009

REFERENCES

1. Qi L, Wei Y, Xu L, Liu Z. Reaction behaviors and kinetics during induction period of methanol conversion on HZSM-5 zeolite. *ACS Catal*. 2015;5(7):3973-3982.
2. Ma D, Shu Y, Cheng M, Xu Y, Bao X. On the induction period of methane aromatization over Mo-based catalysts. *J Catal*. 2000;194(1):105-114.
3. Schilstra MJ, Veldink GA, Vliegenthart JF. Kinetic analysis of the induction period in lipoxygenase catalysis. *Biochemistry*. 1993;32(30):7686-7691.
4. Xia K, Lang W-Z, Li P-P, Yan X, Guo Y-J. Analysis of the catalytic activity induction and deactivation of PtIn/Mg(Al)O catalysts for propane dehydrogenation reaction. *RSC Adv*. 2015;5(79):64689-64695.
5. Seriani N. Ab initiothermodynamics of lithium oxides: from bulk phases to nanoparticles. *Nanotechnology*. 2009;20(44):445703.
6. de Smit E, Cinquini F, Beale AM, et al. Stability and reactivity of epsilon-chi-theta iron carbide catalyst phases in Fischer-Tropsch synthesis: controlling mu(c). *J Am Chem Soc*. 2010;132(42):14928-14941.
7. Thuinet L, Besson R. Ab initio study of competitive hydride formation in zirconium alloys. *Intermetallics*. 2012;20(1):24-32.
8. Walsh A, Chen S, Wei S-H, Gong X-G. Kesterite thin-film solar cells: advances in materials modelling of Cu_2ZnSnS_4. *Adv Energy Mater*. 2012;2(4):400-409.

9. Weckhuysen BM. Snapshots of a working catalyst: possibilities and limitations of in situ spectroscopy in the field of heterogeneous catalysis. *Chem Commun*. 2002;(2):97-110. https://doi.org/10.1039/B107686H
10. Catalysis as it goes. *Nat Catal*. 2018;1(3):165-166.
11. Reuter K, Scheffler M. Composition, structure, and stability of RuO_2(110) as a function of oxygen pressure. *Phys Rev B*. 2001;65(3):035406.
12. Reuter K, Scheffler M. Composition and structure of the RuO_2(110) surface in an O_2 and CO environment: implications for the catalytic formation of CO_2. *Phys Rev B*. 2003;68(4):045407.
13. Reuter K, Scheffler M. First-principles atomistic thermodynamics for oxidation catalysis: surface phase diagrams and catalytically interesting regions. *Phys Rev Lett*. 2003;90(4):046103.
14. Reuter K. Ab initio thermodynamics and first-principles microkinetics for surface catalysis. *Catal Lett*. 2016;146(3):541-563.
15. Wang T, Wang S, Li Y-W, Wang J, Jiao H. Adsorption equilibria of CO coverage on β-Mo_2C surfaces. *J Phys Chem C*. 2012;116(10):6340-6348.
16. Prodhomme P-Y, Raybaud P, Toulhoat H. Free-energy profiles along reduction pathways of MoS_2 M-edge and S-edge by dihydrogen: a first-principles study. *J Catal*. 2011;280(2):178.
17. Senftle TP, Carter EA. Theoretical determination of band edge alignments at the water–$CuInS_2$(112) semiconductor interface. *Langmuir*. 2017;33(37):9479-9489.
18. Sai Gautam G, Senftle TP, Carter EA. Understanding the effects of cd and Ag doping in Cu_2ZnSnS_4 solar cells. *Chem Mater*. 2018;30(14):4543-4555.
19. Frenkel D, Smit B. *Understanding Molecular Simulation: From Algorithms to Applications*. 2nd ed. Elsevier; 2002.
20. Wolf RJ, Lee MW, Davis RC, Fay PJ, Ray JR. Pressure-composition isotherms for palladium hydride. *Phys Rev B*. 1993;48(17):12415-12418.
21. Wolf RJ, Lee MW, Ray JR. Pressure-composition isotherms for nanocrystalline palladium hydride. *Phys Rev Lett*. 1994;73(4):557-560.
22. Lee MW, Wolf RJ, Ray JR. Atomistic calculations of hydrogen loading in palladium. *J Alloys Compd*. 1995;231(1):343-346.
23. Lachet V, Boutin A, Tavitian B, Fuchs AH. Grand canonical Monte Carlo simulations of adsorption of mixtures of xylene molecules in faujasite zeolites. *Faraday Discuss*. 1997;106(0):307-323.
24. Senftle TP, Hong S, Islam MM, et al. The ReaxFF reactive force-field: development, applications and future directions. *Npj Comput Mater*. 2016;2(1):1-14.
25. Senftle TP, Meyer RJ, Janik MJ, van Duin ACT. Development of a ReaxFF potential for Pd/O and application to palladium oxide formation. *J Chem Phys*. 2013;139(4):044109.
26. Senftle TP, van Duin ACT, Janik MJ. Methane activation at the Pd/-CeO_2 Interface. *ACS Catal*. 2017;7(1):327-332.
27. Senftle TP, Janik MJ, van Duin ACT. A ReaxFF investigation of hydride formation in palladium nanoclusters via Monte Carlo and molecular dynamics simulations. *J Phys Chem C*. 2014;118(9):4967-4981.
28. Senftle TP, van Duin ACT, Janik MJ. Determining in situ phases of a nanoparticle catalyst via grand canonical Monte Carlo simulations with the ReaxFF potential. *Catal Commun*. 2014;52:72-77.
29. Fantauzzi D, Krick Calderón S, Mueller JE, et al. Growth of stable surface oxides on Pt(111) at near-ambient pressures. *Angew Chem Int Ed*. 2017;56(10):2594-2598.
30. Kirchhoff B, Braunwarth L, Jung C, Jónsson H, Fantauzzi D, Jacob T. Simulations of the oxidation and degradation of platinum electrocatalysts. *Small*. 2020;16(5):1905159.
31. Gai L, Shin YK, Raju M, van Duin ACT, Raman S. Atomistic adsorption of oxygen and hydrogen on platinum catalysts by hybrid grand canonical Monte Carlo/reactive molecular dynamics. *J Phys Chem C*. 2016;120(18):9780-9793.
32. Wexler RB, Qiu T, Rappe AM. Automatic prediction of surface phase diagrams using ab initio grand canonical Monte Carlo. *J Phys Chem C*. 2019;123(4):2321-2328.
33. Collett CH, McGregor J. Things go better with coke: the beneficial role of carbonaceous deposits in heterogeneous catalysis. *Cat Sci Technol*. 2016;6(2):363-378.
34. Zhang R, Liu H, Li Q, Wang B, Ling L, Li D. Insight into the role of the promoters Pt, Ru and B in inhibiting the deactivation of Co catalysts in Fischer-Tropsch synthesis. *Appl Surf Sci*. 2018;453:309-319.
35. Xu J, Saeys M. Improving the coking resistance of Ni-based catalysts by promotion with subsurface boron. *J Catal*. 2006;242(1):217-226.
36. Tsakoumis NE, Rønning M, Borg Ø, Rytter E, Holmen A. Deactivation of cobalt based Fischer–Tropsch catalysts: a review. *Catal Today*. 2010;154(3):162-182.
37. Kim WY, Jang JS, Ra EC, Kim KY, Kim EH, Lee JS. Reduced perovskite $LaNiO_3$ catalysts modified with Co and Mn for low coke formation in dry reforming of methane. *Appl Catal Gen*. 2019;575:198-203.
38. Koo KY, Roh H-S, Jung UH, Seo DJ, Seo Y-S, Yoon WL. Combined H_2O and CO_2 reforming of CH_4 over nano-sized Ni/MgO-Al_2O_3 catalysts for synthesis gas production for gas to liquid (GTL): effect of Mg/Al mixed ratio on coke formation. *Catal Today*. 2009;146(1):166-171.
39. Souza MMVM, Aranda DAG, Schmal M. Coke formation on Pt/-ZrO_2/Al_2O_3 catalysts during CH_4 reforming with CO_2. *Ind Eng Chem Res*. 2002;41(18):4681-4685.
40. Al-Fatish ASA, Ibrahim AA, Fakeeha AH, Soliman MA, Siddiqui MRH, Abasaeed AE. Coke formation during CO_2 reforming of CH_4 over alumina-supported nickel catalysts. *Appl Catal Gen*. 2009;364(1):150-155.
41. Horváth A, Stefler G, Geszti O, Kienneman A, Pietraszek A, Guczi L. Methane dry reforming with CO_2 on CeZr-oxide supported Ni, NiRh and NiCo catalysts prepared by sol–gel technique: relationship between activity and coke formation. *Catal Today*. 2011;169(1):102-111.
42. Olahová N, Symoens SH, Djokic MR, et al. CoatAlloy barrier coating for reduced coke formation in steam cracking reactors: experimental validation and simulations. *Ind Eng Chem Res*. 2018;57(3):897-907.
43. Schietekat CM, Sarris SA, Reyniers PA, et al. Catalytic coating for reduced coke formation in steam cracking reactors. *Ind Eng Chem Res*. 2015;54(39):9525-9535.
44. Tan S, Hu B, Kim W-G, et al. Propane dehydrogenation over alumina-supported iron/phosphorus catalysts: structural evolution of iron species leading to high activity and propylene selectivity. *ACS Catal*. 2016;6(9):5673-5683.
45. Wang H-Z, Sun L-L, Sui Z-J, et al. Coke formation on Pt–Sn/Al_2O_3 catalyst for propane dehydrogenation. *Ind Eng Chem Res*. 2018;57(26):8647-8654.
46. Sun Y, Wu Y, Shan H, Wang G, Li C. Studies on the promoting effect of sulfate species in catalytic dehydrogenation of propane over Fe_2O_3/Al_2O_3 catalysts. *Cat Sci Technol*. 2015;5(2):1290-1298.
47. Sun Y, Tao L, You T, Li C, Shan H. Effect of sulfation on the performance of Fe_2O_3/Al_2O_3 catalyst in catalytic dehydrogenation of propane to propylene. *Chem Eng J*. 2014;244:145-151.
48. Hill JM, Cortright RD, Dumesic JA. Silica- and L-zeolite-supported Pt, Pt/Sn and Pt/Sn/K catalysts for isobutane dehydrogenation. *Appl Catal Gen*. 1998;168(1):9-21.
49. Ma R, Yang T, Gao J, et al. Composition tuning of Ru-based phosphide for enhanced propane selective dehydrogenation. *ACS Catal*. 2020;10(17):10243-10252.
50. Watanabe R, Hirata N, Fukuhara C. Active species of sulfated metal oxide catalyst for propane dehydrogenation. *J Jpn Pet Inst*. 2017;60(5):223-231.
51. Watanabe R, Hirata N, Miura K, Yoda Y, Fushimi Y, Fukuhara C. Formation of active species for propane dehydrogenation with hydrogen

sulfide co-feeding over transition metal catalyst. *Appl Catal Gen*. 2019;587:117238.
52. Wang G, Li C, Shan H. Highly efficient metal sulfide catalysts for selective dehydrogenation of Isobutane to isobutene. *ACS Catal*. 2014;4(4):1139-1143.
53. Neylon MK, Choi S, Kwon H, Curry KE, Thompson LT. Catalytic properties of early transition metal nitrides and carbides: n-butane hydrogenolysis, dehydrogenation and isomerization. *Appl Catal Gen*. 1999;183(2):253-263.
54. Cortright RD, Hill JM, Dumesic JA. Selective dehydrogenation of isobutane over supported Pt/Sn catalysts. *Catal Today*. 2000;55(3):213-223.
55. Ma Z, Wu Z, Miller JT. Effect of Cu content on the bimetallic Pt–Cu catalysts for propane dehydrogenation. *Catal Struct React*. 2017;3(1–2):43-53.
56. Wegener EC, Wu Z, Tseng H-T, et al. Structure and reactivity of Pt–In intermetallic alloy nanoparticles: highly selective catalysts for ethane dehydrogenation. *Catal Today*. 2018;299:146-153.
57. Sattler JJHB, Ruiz-Martinez J, Santillan-Jimenez E, Weckhuysen BM. Catalytic dehydrogenation of light alkanes on metals and metal oxides. *Chem Rev*. 2014;114(20):10613-10653.
58. National Academies of Sciences, Engineering, and Medicine. *The Changing Landscape of Hydrocarbon Feedstocks for Chemical Production: Implications for Catalysis: Proceedings of a Workshop*. National Academies Press; 2016.
59. Barias OA, Holmen A, Blekkan EA. Propane dehydrogenation over supported Pt and Pt-Sn catalysts: catalyst preparation, characterization, and activity measurements. *J Catal*. 1996;158(1):1-12.
60. Hu B, Schweitzer NM, Zhang G, et al. Isolated Fe^{II} on silica as a selective propane dehydrogenation catalyst. *ACS Catal*. 2015;5(6):3494-3503.
61. Sun Y, Wu Y, Tao L, Shan H, Wang G, Li C. Effect of pre-reduction on the performance of Fe_2O_3/Al_2O_3 catalysts in dehydrogenation of propane. *J Mol Catal Chem*. 2015;397:120-126.
62. Sarazen ML, Jones CW. MOF-derived iron catalysts for nonoxidative propane dehydrogenation. *J Phys Chem C*. 2018;122(50):28637-28644.
63. Wang P, Senftle TP. Theoretical insights into non-oxidative propane dehydrogenation over Fe_3C. *Phys Chem Chem Phys*. 2021;23(2):1401-1413.
64. Armbrüster M, Kovnir K, Friedrich M, et al. $Al_{13}Fe_4$ as a low-cost alternative for palladium in heterogeneous hydrogenation. *Nat Mater*. 2012;11(8):690-693.
65. Piccolo L. $Al_{13}Fe_4$ selectively catalyzes the hydrogenation of butadiene at room temperature. *Chem Commun*. 2013;49(80):9149-9151.
66. Pan JL, Ni J, Yang B. Stability of FeAl(110) alloy surface structures: a first-principles study. *Eur Phys J B*. 2010;73(3):367-373.
67. van Duin ACT, Dasgupta S, Lorant F, Goddard WA. ReaxFF: a reactive force field for hydrocarbons. *J Phys Chem A*. 2001;105(41):9396-9409.
68. Behler J. Perspective: machine learning potentials for atomistic simulations. *J Chem Phys*. 2016;145(17):170901.
69. Wrobel RJ, Hełminiak A, Arabczyk W, Narkiewicz U. Studies on the kinetics of carbon deposit formation on nanocrystalline iron stabilized with structural promoters. *J Phys Chem C*. 2014;118(28):15434-15439.
70. Zhang L, Hou P-X, Li S, et al. In situ TEM observations on the sulfur-assisted catalytic growth of single-wall carbon nanotubes. *J Phys Chem Lett*. 2014;5(8):1427-1432.
71. Henkelman G, Arnaldsson A, Jónsson H. A fast and robust algorithm for Bader decomposition of charge density. *Comput Mater Sci*. 2006;36(3):354-360.

SUPPORTING INFORMATION

Additional supporting information may be found in the online version of the article at the publisher's website.

How to cite this article: Wang P, Senftle TP. Modeling phase formation on catalyst surfaces: Coke formation and suppression in hydrocarbon environments. *AIChE J*. 2021;67(12):e17454. doi:10.1002/aic.17454